Title: Rolling of soft microbots with tunable traction

Authors: Yan Gao, ¹ Brennan Sprinkle², Ela Springer, ³ David W. M. Marr, ^{3,*} and Ning Wu^{3,*}

Affiliation: ¹Materials Science and Engineering Program, Colorado School of Mines, Golden, United States of America.

²Department of Applied Mathematics and Statistics, Colorado School of Mines, Golden, United States of America.

³Department of Chemical and Biological Engineering, Colorado School of Mines, Golden, United States of America.

Corresponding authors: dmarr@mines.edu (David W. M. Marr) and ningwu@mines.edu (Ning Wu)

One sentence summary: Inspired by tank treading, we show that soft microbots based on deformable Pickering emulsions exhibit tractions much higher than their rigid counterparts, overcoming the limitations of low translation efficiency and drug loading capacity associated with rigidity.

Abstract

Microbot (µbot)-based targeted drug delivery has attracted increasing attention due to its potential for avoiding side effects associated with systemic delivery. To date, most ubots have been fabricated from rigid materials which can have issues of biocompatibility and challenges with incorporating drugs. In addition, hard ubots that roll on surfaces have significant slip due to the presence of a liquid lubrication layer. Here, we introduce magnetically-controlled soft ubot rollers based on Pickering emulsions that, due to their intrinsic deformability, fundamentally change the nature of the lubrication layer and roll like deflated tires. With a large contact area between ubot and wall, soft ubots exhibit tractions much higher than their rigid counterparts, results we support with both theoretical analysis and numerical simulation. In addition, we show that the magnetic particle distribution at the microbot interface can be reconfigured with the external field. Upon superposition of alternating- and direct-current magnetic fields, particles accumulate at the equator while redistributing toward the poles when the direct-current field is removed. This reconfiguration of surface particles strongly influences both the translation speed and traction. Finally, we demonstrate that these Pickering emulsionbased ubots can be destabilized with external stimuli such as pH and used to deliver their contents to a desired location, potentially overcoming the limitations of low translation efficiency, biocompatibility, and drug loading capacity associated with rigid structures.

Introduction

External control of microscale robots has attracted significant interest because of the desire to direct *in vivo* devices (1,2). However, compared with microbot (μbot) manipulation methods such as chemical (3,4), electric (5,6), light (7,8), or acoustic techniques (9), magnetic actuation methods have several advantages, including non-invasiveness, fast response times, high directionality (10), and excellent biocompatibility (11). As a result, magnetic field-assisted drug delivery efforts can be traced back to the '80s (11,12), with now multiple magnetic μbot approaches developed (13), including helical swimmers (14), microwalkers (15), undulating chains (16), flapping nanomagnets (17), reconfigurable swarms (18), and surface rollers (19).

Unlike microscopic swimmers, rolling µbots use friction with available surfaces to move. Hard µbots (20) in liquid media, however, roll differently than in dry environments because a liquid lubrication layer between the µbot and wall leads to significant slip. Indeed, lubrication theory predicts that a rigid rolling microsphere must slip near a solid substrate with a maximum rolling velocity of only 1/4th the speed with no slip present (21). Overcoming this theoretical limit requires new approaches if efficient microscale locomotion is to be achieved, an issue particularly important for microenvironments where the surface-to-volume ratios are high. Inspired by tank treading, where a large and flat contact area faces the translation surface without slip, we introduce soft µbots based on Pickering emulsions stabilized by magnetic particles. These fully and partially covered emulsion droplets deform near walls, roll like deflated tires, and interestingly, exhibit larger traction and translate faster than their rigid counterparts. In addition, the particle distribution at the emulsion droplet surface can be reconfigured

using different combinations of alternating-current (AC) and direct-current (DC) magnetic fields to enable direct control of droplet traction. Finally, pH-triggered destabilization of the µbots is demonstrated as a potential approach to targeted delivery. Due to their softness and the liquid core, our soft µbots have the potential for increased biocompatibility, high drug loading capacity, and enhanced transport through physical constraints that may exist *in vivo* (22-25).

Results and Discussion

High traction of deformable droplets

To make them amphiphilic, we first coat the surfaces of carboxyl-functionalized superparamagnetic microparticles with decylamine. As shown in Fig. S1, successful attachment is confirmed with peaks in the FTIR spectra appearing at 2850 cm $^{-1}$ (C–H stretch) and 725 cm $^{-1}$ (C–H rock bond). The zeta potentials are also changed from -60 ± 5 mV to -35 ± 4 mV upon surface modification. We then produce stable Pickering oil-inwater (o/w) emulsions by homogenizing the particle, decane, and water mixture. Depending on the homogenization speed and initial particle concentration, the surface coverage of particles can be tuned from 30% to 100% with a broad size distribution (Fig. 1A). The fabricated Pickering emulsions remain stable for at least several months, allowing us to investigate their actuation under magnetic fields conveniently.

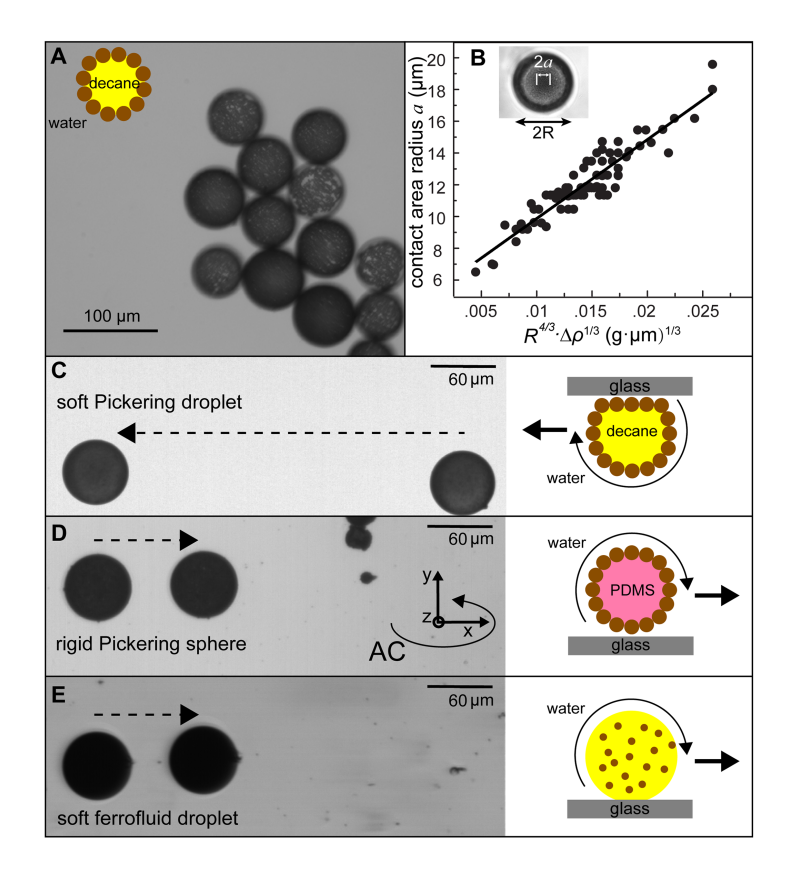


Figure. 1 (A) Pickering decane-in-water emulsion droplets are partially or fully covered with modified 1 μ m polystyrene-Fe₃O₄ composite beads. (B) The contact area radius a of the droplets depends on their radius R. Fit is based on Eq. (1). Inset: the image of a deformed droplet. Rolling of a (C) soft Pickering droplet, (D) a rigid Pickering sphere, and (E) a soft ferrofluid droplet over 8.5 s under a rotating magnetic field ($H_0 = 2.5$ mT and f = 20 Hz) along the x-z plane.

Since decane is lighter than water, droplets float to the top slide and deform due to their softness. Under high magnification, the circular contact area can be clearly seen (Fig. 1B inset) with all particles in focus within the contact plane (Fig. S2). The contact area radius is governed by the Hertzian model (34), where the droplet deforms due to the competition between buoyancy and elastic forces

$$a = \left(\frac{3WR}{4E}\right)^{\frac{1}{3}} = \left(\frac{\pi g \Delta \rho}{E}\right)^{\frac{1}{3}} R^{\frac{4}{3}} \tag{1}$$

with W the buoyancy force, g the gravitational constant, and $\Delta \rho$ the density difference between water and droplets consisting of decane and surface magnetic particles. E is the effective stiffness between the elastic properties of two materials

$$\frac{1}{E} = \frac{1 - v_1^2}{E_1} + \frac{1 - v_2^2}{E_2} \tag{2}$$

where v_1 and v_2 are the Poisson's ratios and E_1 and E_2 are Young's moduli of the droplet and glass slide, respectively. In our experiments (Fig. 1B), we find that the contact area radius a is independent of the particle surface coverage and scales as $a \propto R^{4/3}$ as expected from Eq. (1). The impact of droplet radius and surface particles on the droplet density (35) has been included in the original Hertzian model calculations in Fig. 1B. Based on Eq. (2), we calculate the effective Young's modulus of droplets $E_1 \sim 139$ Pa, consistent with literature values for Pickering emulsions (36). This agreement also indicates that the adhesion force between the droplet and glass slide is negligible because a would otherwise scale with a (37). Moreover, when we tilt the glass slide a volume a would off, confirming that the adhesive force is minimal.

The softness and deformability of Pickering droplets significantly impact their rolling behavior. Here, we apply a two-dimensional (2D) rotating magnetic field (Fig. S3) along the x-z plane, $H = H_0(cos\omega_M t\hat{x} + sin\omega_M t\hat{z})$, where H_0 is the field strength and $f = \omega_M/2\pi = 20$ Hz is the field frequency. Note that the step-out frequency of the soft droplets is 1-3 Hz which decreases with increasing droplet radius. As with our previous work on μ bots assembled from hard beads (38), soft droplets roll because of the broken symmetry in hydrodynamics near the top glass slide (Fig. 1C and Movie S1). Movie S2 also shows that the contact area of the static and rolling droplets remains constant. Here, the droplet surface particles produce a tank-treading motion and roll like a deflated tire.

For comparison, we study analogous rigid µbots by replacing the liquid core with crosslinked PDMS while retaining the outer particle shell, expecting an elastic modulus ~26,000 times greater than the soft ones (39). Although these rigid spheres are heavier than the water medium and settle to the bottom glass substrate, no deformation can be observed. Under identical fields, these rigid Pickering spheres roll like fully inflated tires; however, they roll ~3× more slowly than soft droplets (Fig. 1D and Movie S1) even though they are of similar size and have the same magnetic particle surface coverage. Note that the translation direction of the rigid sphere is opposite the Pickering droplet because one is adjacent to the bottom substrate while the other floats to the top.

For further comparison, we have fabricated soft droplets with a ferrofluid liquid core composed of 5 wt% 10 nm Fe₃O₄ nanoparticles. These roll at a similar speed as rigid Pickering spheres, ~3× slower than the soft Pickering droplets. Soft ferrofluid droplets roll slowly because the magnetic nanoparticles are suspended in the droplet and are free to rotate in the liquid core under applied fields. As a result, the net torque transmitted to the droplet is small because of viscous dissipation. Therefore, although the magnetic particle loading in the ferrofluid droplet is much higher than in the Pickering droplet, it is not a very efficient μbot. The difference in speed between rigid and soft spheres in Fig. 1C-D, however, poses interesting questions regarding the role of deformation in μbot translation.

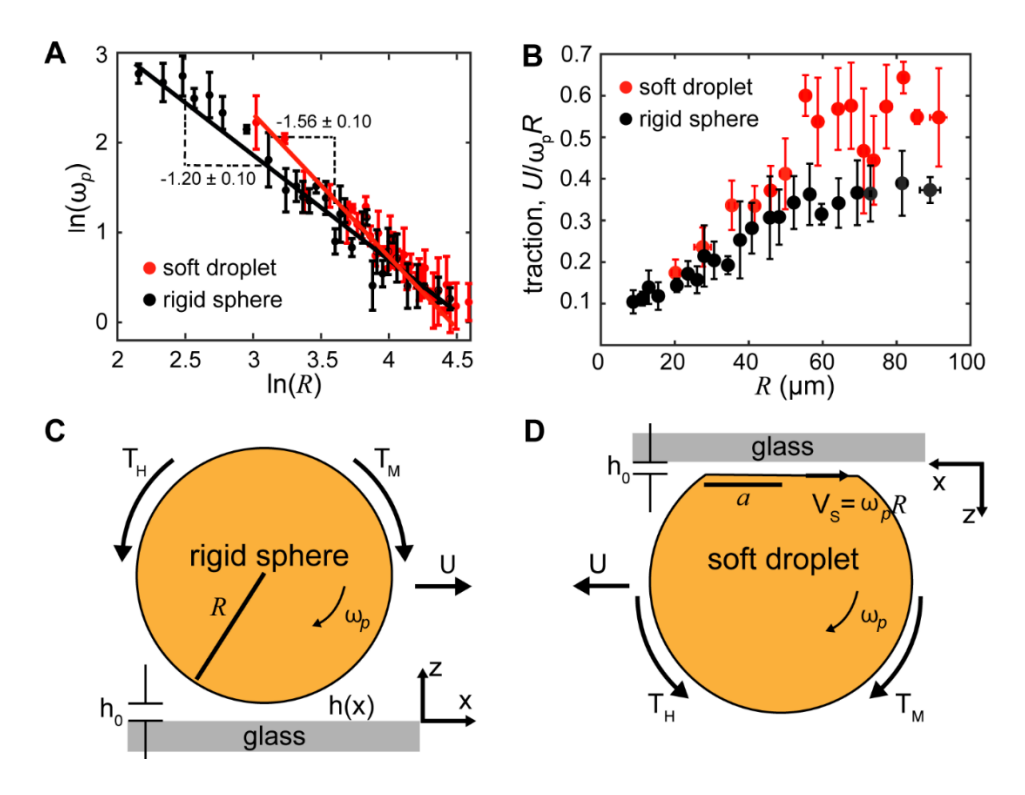


Figure 2. (A) Angular velocities of rigid and soft Pickering droplets under identical magnetic fields ($H_0 = 2.5 \text{ mT}$ and f = 20 Hz) with the slopes of the fitted lines indicated. (B) Tractions of rigid and soft Pickering droplets. The error bars in (A) and (B) around each data point are determined from five different measurements. Schematic of a (C) rigid sphere and (D) soft droplet rolling under an AC magnetic field. T_H and T_M are the hydrodynamic and magnetic torques. Surface particles in both cases are not shown for simplicity.

To fully characterize the rolling of soft and rigid Pickering droplets, we measure the translational U and angular rotation ω_p velocities for different droplet sizes with 100% surface coverage. Minor but visible defects in surface particle packing allow for accurate tracking of rotation rates. The dependence of the droplet velocity on radius and actuation frequency is shown in Fig. S4. As shown in Figs. 2A-B, the angular velocities of soft and rigid droplets show different size dependencies, with the traction of soft droplets higher than that of solid ones. Here, we define the traction $\gamma = U/\omega_p R$ as a means of characterizing rolling; a value of $\gamma = 1$ corresponds to no slip, while μ bots with $\gamma = 0$ would not translate.

The rolling behavior of rigid droplets can be understood by classical hydrodynamic lubrication theory (21). In this, the hydrodynamic torque T_H consists of torques due to translation and rotation

$$T_H = T_H^t + T_H^r = 8\pi R^3 \eta \omega (T_H^{r*} + \gamma T_H^{t*})$$
 (3)

where η is the solvent viscosity. When the separation between the sphere and the wall is small $(h_0/R \ll 1)$, the correction factors T_H^{t*} and T_H^{r*} can be expressed as

$$T_H^{r*} = \frac{2}{5} ln\left(\frac{h_0}{R}\right) - 0.3817 \text{ and } T_H^{t*} = -\frac{1}{10} ln\left(\frac{h_0}{R}\right) - 0.1895$$
 (4)

The magnetic torque T_M is the sum of torques generated on all surface particles

$$T_{\mathbf{M}} = \langle \mu_{S} \mathbf{m} \times \mathbf{H} \rangle N_{p} \mu_{S} \chi^{"} V_{0} H_{0}^{2} = 4R^{2} \mu_{S} \chi^{"} V_{0} H_{0}^{2} / r_{p}^{2} \, \mathbf{\hat{y}}$$

$$\tag{5}$$

where $\langle \cdot \rangle$ corresponds to the average over one period of the rotating field. **m** is the magnetic dipole moment of one particle, **H** is the applied field, and μ_s is the solvent permeability. $N_p = 4\pi R^2/\pi r_p^2$ is the total number of particles on the droplet surface where r_p is the radius of the magnetic particle. The imaginary part of the magnetic susceptibility χ'' characterizes the phase lag between the induced dipole and the field which generates the torque. V_θ is the volume of one particle and H_θ is the field strength.

At steady state, the balance between the hydrodynamic and magnetic torques yields a scaling between the angular velocity and the droplet size $\omega_p \propto R^{-1}[-ln(h_0/R)]^{-1} \approx R^{-1.36}$ (Section S1 and Fig. S5) close to the scaling $\omega_p \propto R^{-1.2}$ observed in experimental measurements (Fig. 2A). Minor discrepancies can be explained by the neglect of the pressure force within the lubrication layer, which effectively makes the gap h_0 larger than expected from a balance of gravitational and electrostatic forces only.

Fig. 2B shows that rigid droplets have lower traction than soft ones. In this, the entrained thin liquid film between the wall and rigid sphere acts as an effective lubrication layer, making the rolling inefficient. However, the situation is different for soft droplets which deform and maintain a significant Hertzian contact area with the wall (Fig. 2D). Unlike the wedge-shaped liquid film h(x) between the rigid droplet and the wall, the confined liquid for soft droplets has an almost constant thickness h_0 extending across the entire contact area, making the lubrication effect only dominant in the regions near the contact edges (40). Moreover, because $a \gg h_0$, we can safely assume that the net flux of fluid within the gap, $q = \int_0^{h_0} v_x dz$, where v_x is the fluid velocity along the x-axis within the gap, is very small. Therefore, any volume of fluid displaced by the droplet is assumed to flow around the droplet away from the wall rather than through the gap. After solving the velocity profile within the gap and equating the shear and pressure forces for the soft droplet, we can conclude (Section S2 in SI) that the difference between the droplet translation velocity U and the tank treading velocity of surface particles $V_s = \omega_p R$ is small:

$$U - V_s = U - \omega_p R = 2 \, q / h_0. \tag{6}$$

This explains the large traction observed in soft droplets. An additional impact of μ bot deformability is that the Hertzian contact can make the droplet very compliant with the substrate. As a result, the liquid flux within the gap may be extremely small, approaching the limit of dry friction with no slip. Therefore, the softness of the μ bots can have a profound impact on the rolling of μ bots.

Numerical simulation

To further corroborate our theoretical analysis, we also performed numerical simulations where the droplet softness can be varied directly. Due to constraints in computational time, we choose droplets with a range of sizes between $R = 4.61 \, \mu m - 19.78 \, \mu m$ whose surfaces are densely covered by N_p 1- μ m diameter particles (e.g., N_p = 252 for $R = 4.61 \, \mu m$ and $N_p = 4002$ for $R = 19.78 \, \mu m$). Here, R is reported without including particle size; therefore, the outermost radius of a droplet is $R_0 = R + 0.5 \, \mu m$ assuming particles are located with their mid-planes at the liquid-liquid interface. While the droplet sizes we consider are typically smaller than those used in our experiments, they are sufficient to investigate the effect of droplet softness on translation and traction since the ratios of the contact area to droplet radii are comparable to the larger droplets. Furthermore, numerical simulations allow us to decouple the softness of a droplet from its size and independently investigate its effects on droplet traction. To study the effect of droplet softness on locomotion, we vary the dimensionless contact radius

$$\overline{a} = \frac{a}{2r_p} = \left(\frac{3N_p m_e gR}{4\kappa_{hend}}\right)^{1/3} \tag{7}$$

where m_e is the effective mass of the particles and κ_{bend} is the effective bending modulus of the droplet, whose deformation is primarily controlled by the balance between κ_{bend} and gravitational energy. A softer droplet with a smaller κ_{bend} or a larger R has a larger dimensionless contact radius \overline{a} . In our simulations, we consider the following forces on the group of particles straddling the surface of a Pickering droplet of radius R: the magnetic force F^{mag} that drives the droplets, the hydrodynamic force F^{hydro} , the interfacial forces $F^{tension}$ and F^{bend} that constrain the particles to the interface and capture the droplet softness, and the gravitational force F^{grav} that balances F^{bend} to

control deformation against the wall. The detailed expressions of those forces, our simulation method, and a table of parameters used to match experimental conditions can be found in the Materials and Methods section.

Each of our simulations begins with an initially spherical droplet formed by vertices on an icosphere (41) where particles are spaced approximately $2r_p$ apart and equilibrated with no applied magnetic force over 0.25 s to allow for elastic deformation due to gravitation. For convenience, we make the droplet heavier than the medium so it settles and rolls on the bottom substrate. Fig. 3A and Movie S3 show the rolling of rigid and softer droplets of the same size ($R = 9.6 \mu m$) in 2 s. Particles around the droplet equator are darkened to provide a visual indication of the droplet orientation. The softer green droplet ($\overline{a} = 2.43$) rolls 3.5× faster than the blue rigid droplet ($\overline{a} = 1.09$), leading to tractions of $\gamma = 0.26$ vs. $\gamma = 0.074$. These values are consistent with our experimental values for small ($R \le 10 \mu m$) rigid droplets, although we cannot make soft droplets smaller than 10 μm with 1 μm magnetic particles.

Fig. 3B shows results from our numerical studies on the simulated droplet traction $\gamma = U/\omega_p R$ as a function of dimensionless contact radius \overline{a} . The error bars show the spread in traction values we observe by using different parameter values representing the same value of \overline{a} , with details provided in the Materials and Methods section. The low variance in the error bars demonstrates that droplet traction is primarily controlled by the dimensionless softness \overline{a} . Here, we vary \overline{a} both by fixing R = 4.61 µm and changing κ_{bend} (Fig. 3C) and by fixing κ_{bend} while changing R (Fig. 3D). Fig. 3B shows that increasing \overline{a} for a fixed droplet size (solid black curve) monotonically increases the droplet's traction γ . The inset of Fig. 3B shows how far six representative droplets with fixed size

but different κ_{bend} have traveled over a 2 s interval. Here, the softer droplets travel faster and have larger traction than more rigid ones. The softer droplet results in a larger traction of $\gamma = 0.18$, nearly $2 \times$ faster than the equal-sized rigid droplet with $\gamma = 0.089$ and consistent with the experimentally observed trend in traction values for increasingly soft droplets. However, beyond roughly $\overline{a} = 2.1$, the rate of increase in γ begins to slow due to finite size effects from the fixed droplet size. By increasing \overline{a} using the droplet radius instead (dashed black line), we avoid finite size effects at the cost of more expensive computations, however, we also see agreement between the two curves around $\overline{a} = 2.1$ indicating that any method of varying \overline{a} (droplet size or κ_{bend}) produces the correct trend in γ so long as finite size limitations are avoided. Although the current simulation method prevents us from simulating even larger droplets within a reasonable amount of time, the black dashed curve in Fig. 3B show that the traction increases with droplet size, consistent with experiments, and this trend depends only on the dimensionless Hertzian contact radius \overline{a} .

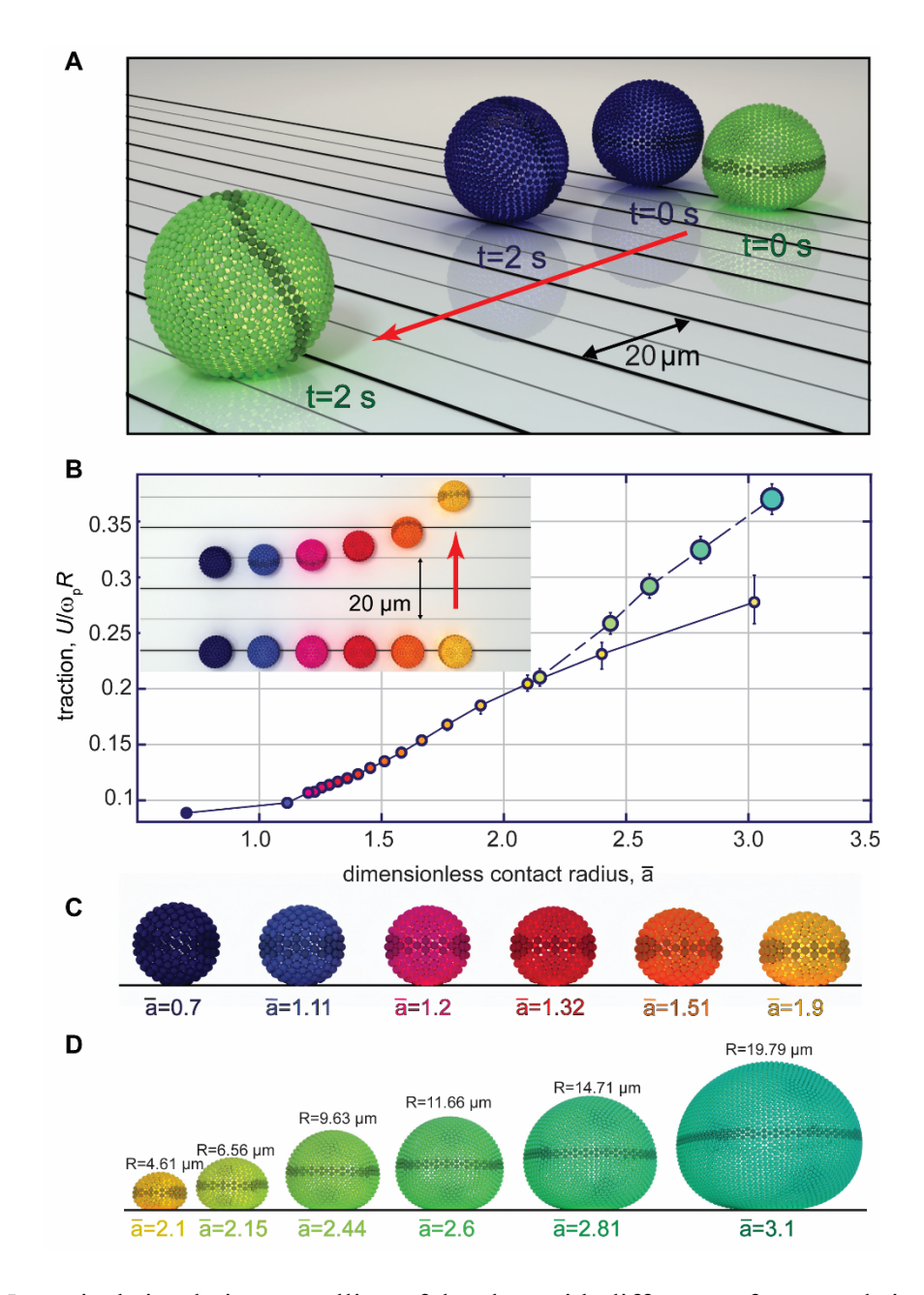


Fig. 3. Numerical simulation on rolling of droplets with different softness and size. (A) Position of larger droplets with R = 9.6 μm at times t = 0 s and t = 2 s. The softer green droplet ($\overline{a} = 2.43$) rolls $3.5 \times$ faster than the blue rigid droplet ($\overline{a} = 1.09$) (Movie S3). Particles around the droplet equator are darkened to provide a visual indication of the droplet orientation. (B) Droplet traction γ vs. dimensionless contact radius \overline{a} . The solid black curve shows the effect of varying \overline{a} for a fixed droplet size R = 4.61 μm, where markers (also of fixed size) are colored from rigid droplets in indigo to soft droplets in yellow. The dashed black curve shows the effect of varying \overline{a} by varying droplet size R where marker sizes vary according to droplet size. Inset: The positions of six representative droplets (top view) with varying \overline{a} at times t = 0 s and t = 2 s. Grid lines on the substrate surface are spaced every 10 μm with the red arrow indicating the rolling direction. (C) Droplet side view equilibrated over 0.25 s with no applied magnetic forces.

All droplets have the same radius $R = 4.61 \mu m$. (D) Droplets with varying R and contact radius \overline{a} varies accordingly.

Traction tuning by reconfiguring the distribution of surface particles

In addition to modifying the traction of soft ubots via their deformability, we can also tune it by reconfiguring the surface particle distribution on partially covered droplets. For example, when we apply a 2D 2.5 mT rotation field along the x-z plane, the initially uniformly distributed particles at 40% surface coverage migrate toward the two poles (Fig. 4A). When we superimpose a 2.5 mT DC field along the y-axis, however, particles redistribute and accumulate at the equator. Here, the redistribution of surface particles is influenced by both the magnetic field and the confinement imposed by the curved interface. As shown in Fig. 4B, spheres located near the equator and the pole experience different dipolar interactions under the two different magnetic fields. When an x-z rotating field is applied, spheres near the equator experience a strong dipolar repulsion (Fig. 4B, red arrows) because the angle θ between the center connector $\mathbf{r}_{ii} = \mathbf{r}_i - \mathbf{r}_i$ and the field **H** is close to 90°. In comparison, spheres near the pole have a θ much smaller than the magic angle of 54.74° and experience a strong dipolar attraction. The situation changes, however, when a strong DC field is superimposed along the y-direction. The DC-field induced dipolar interaction (Fig. 4B, blue arrows) is attractive for spheres near the equator because θ is close to zero, while it is repulsive for particle pairs near the pole. With a strong enough DC field, therefore, particles prefer to accumulate near the equator to maximize their alignment of dipoles with the DC field.

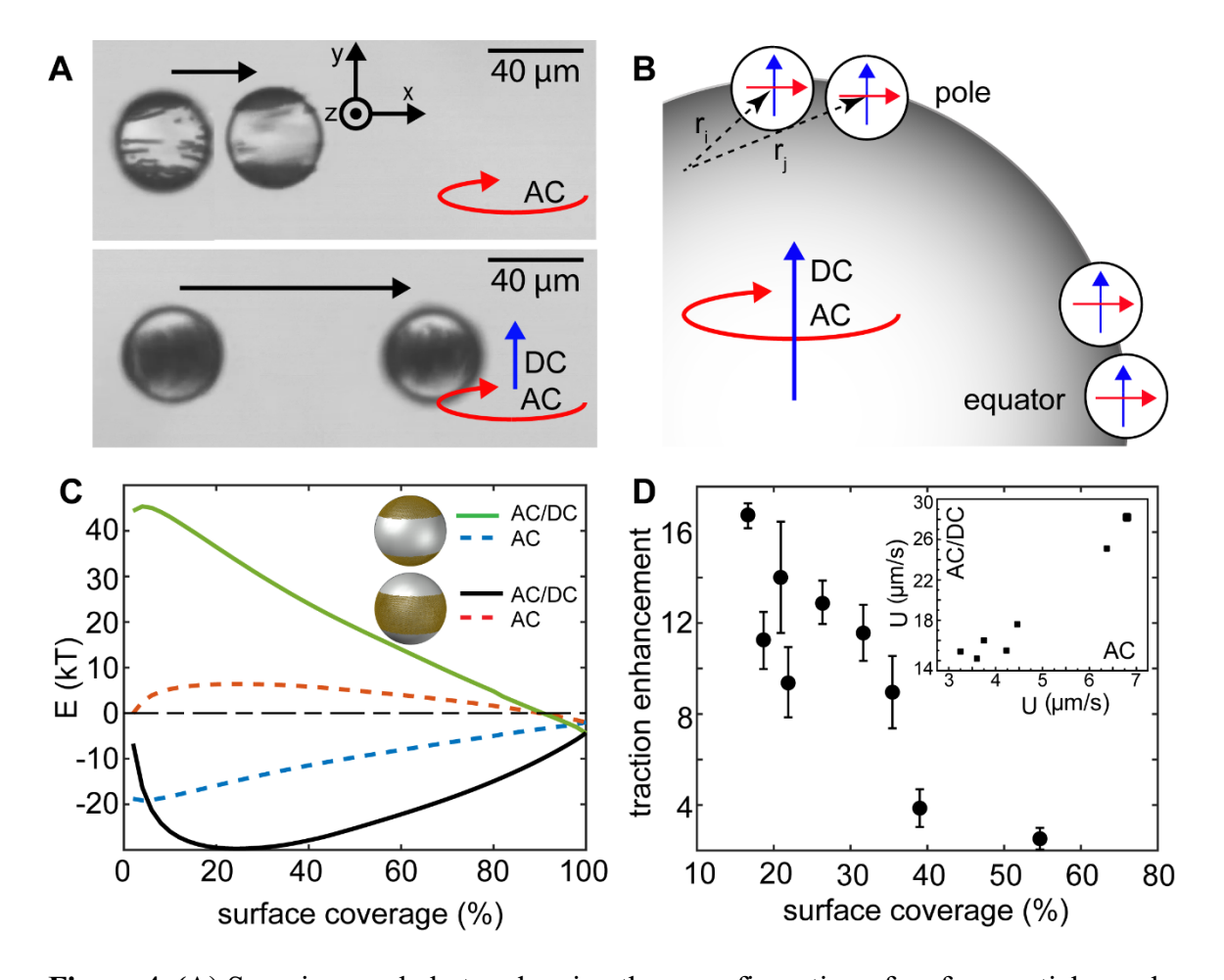


Figure 4. (A) Superimposed photos showing the reconfiguration of surface particles and the difference in velocities under different magnetic fields at a particle surface coverage of 40%. The AC field is 2.5 mT and 20 Hz and the superimposed DC field is 2.5 mT. (B) Illustration of the induced dipoles between neighboring spheres located at the equator and the pole. Red arrows are dipoles induced by the rotating field, while blue arrows are dipoles induced by the DC field. (C) Calculated energies per particle for different magnetic fields and surface particle configurations. (D) Traction enhancement for the equatorial configuration. Inset: Measured velocities at 30% surface coverage. The error bars around each data point are standard deviations determined from five different measurements.

Quantitatively, we can also calculate the total magnetic energies of surface particles with different configurations. Under the combined DC (along the *y*-axis) and AC rotating fields (along the *x-z* plane), $H = H_{xz}cos(\omega_M t)\hat{x} + H_y\hat{y} + H_{xz}sin(\omega_M t)\hat{z}$, the time-averaged pair interaction between spheres *i* and *j* can be expressed as (Section S3 in SI):

$$\langle E_{ij}(r) \rangle = \frac{m_0^2}{4\pi \mu_s r^3 \left[1 - \frac{2\chi'}{3} \left(\frac{r_p}{r} \right)^3 \right]^2} \cdot \left\{ 1 - \frac{3 \left[\left(r^2 - r_y^2 \right) H_{xz}^2 + 2r_y^2 H_y^2 \right]}{2r^2 \left(H_{xz}^2 + H_y^2 \right)} + \left[\left(\frac{1 - \frac{2\chi'}{3} \left(\frac{r_p}{r} \right)^3}{1 + \frac{\chi'}{3} \left(\frac{r_p}{r} \right)^3} \right)^2 - 1 \right] \frac{\left[\left(r^2 + r_y^2 \right) H_{xz}^2 + 2 \left(r^2 - r_y^2 \right) H_y^2 \right]}{2r^2 \left(H_{xz}^2 + H_y^2 \right)} \right\}$$

$$(8)$$

where $m = 4\pi r_p^3 \chi' \mu_s H/3$ is the induced magnetic dipole since the real part of the volume susceptibility χ' is much larger than its imaginary part χ'' , $m_0 = |m|$, r is the separation between particle i and j, $r = |r_{ij}| = (r_x, r_y, r_z)$. The total energies can be calculated by summing the pair interactions over all particles $E = \sum \langle E_{ij} \rangle$. To obtain the coordinates of magnetic particles densely packed onto a spherical interface, we use 3ds Max geosphere with the icosahedron mesh method (42). In this, the distance between particles is chosen to be 1.1 µm to ensure no overlap between neighboring particles. Fig. 4C shows the calculated energies per particle for the polar vs. equatorial configurations at different surface coverage under the two different magnetic fields. Here, the energy is lower for the polar configuration under the 2D rotating field, but the equatorial configuration has lower energies upon the superposition of a DC field. These results are consistent with both experimental observations and the qualitative analysis based on pair interactions. Although the AC and DC field strengths are the same in Fig. 4A, it can be shown that the interaction (Eq. 8) between neighboring particle pairs is lower when accumulated at the equator than at the pole. Because the interaction due to the AC field is time-averaged, while the interaction due to the DC field is static, the magnitudes of those interactions are quantitatively different.

By changing the surface particle distribution, we can effectively tune the traction and speed of rolling droplets. In the fully covered case, droplets can translate at 30 –100 μm/s; however, for sparsely covered droplets with a polar configuration, the propulsion speed can be as low as a few µm/s. Fig. 4A shows that the same droplet with the equatorial configuration translates ~4× faster than the polar configuration (Movie S4). As shown in Fig. 4D, at the same surface coverage, the traction enhancement, the ratio of γ between the equatorial and polar configurations, can be as high as 17. This enhancement can be attributed to two factors. First, the angular rotation speed ω_p of the equatorial configuration is smaller than the polar configuration for the same surface coverage. This is due to the interference of new, orthogonal torques generated by adding a DC component to the applied field, making the droplets wobble during rolling (Movie S5). Thus ω_p is smaller than that with a purely x-z rotating field, where the particles adopt the polar configuration. Even when polar and equatorial droplet configurations roll at the same ω_p , the traction of the equatorial configuration is still much larger. During rolling, the solid magnetic particles accumulated at the equator are adjacent to the wall. Therefore, similar to the fully covered case, its friction force is significantly increased due to Hertzian deformation.

PH-triggered cargo delivery

Soft µbots allow for the encapsulation of soluble cargo within the liquid core.

Compared with rigid µbots, where cargo is typically attached to the µbot surface, the loading in soft µbots is potentially significantly higher. Since the liquid core can be either oil- or water-based, potentially reactive formulations used in targeted drug delivery could be encapsulated. With drug delivery as a potential application, we demonstrate that,

depending on their surface energy, particles can be destabilized for the triggered release of the encapsulants. For example, with a sudden pH increase from 7 to 12, we show in Figs. 5A-D that magnetic surface particles leave the o/w interface as long comet-like tails until the droplets burst (Movie S6). Driving this process is the carboxyl functional groups coated on the particles. They are fully protonated in high pH environments, switching from amphiphilic to hydrophilic and moving into the water phase. As a result, the Laplace pressure can no longer sustain the increase of interfacial tension caused by the loss of surface particles, leading to droplet destabilization. Such a stimulus-triggered delivery mechanism is demonstrated in Movie S7, where the Pickering emulsion droplets roll along at mild pH but destabilize when reaching high pH regions. Here, the droplets are confined within a capillary at pH 7 with tissue paper soaked with pH 13 water plugging one end. Once the droplets reach the end, particles gradually leave the interface destabilizing the bursting droplet.

We note that using pH to trigger the destabilization of µbots and release encapsulants can have potential biomedical applications. For example, it is widely accepted that the pH of cancer cells is slightly acidic compared with normal cells (6.4-7.0 vs. 7.2-7.5) and studies have been performed to make polymeric nanoparticles responsive in this narrow pH range(43). In principle, one can tailor the surface functionalities of the magnetic particles to destabilize them within this pH range. In addition, other means, such as a high-frequency AC magnetic field (e.g., hyperthermia), can also be combined with thermo-responsive polymeric coatings (e.g., poly(N-isopropyl acrylamide)) on the magnetic particles and used as a potential strategy for destabilizing Pickering emulsions and releasing cargo in *in-vivo* environments.

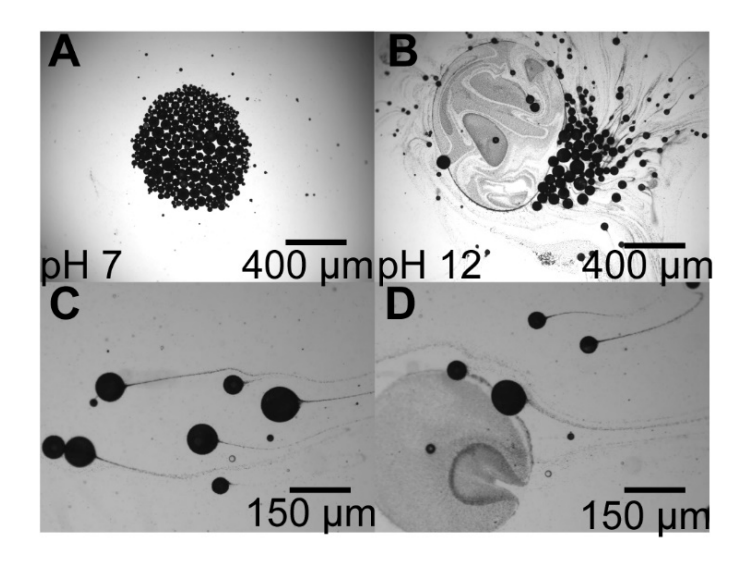


Figure 5. (A) Concentrated Pickering emulsion droplets at pH 7 and (B) at pH 12, where (C) particles leave the droplet interface forming long comet-like tails, eventually causing the droplets to (D) burst.

With regards to other environments and in addition to flat surfaces, soft droplets can translate on curved walls (Fig. S6 and Movie S8). In this, a droplet can roll 90° either clockwise or counterclockwise along a cylindrical capillary, demonstrating its ability to overcome gravity/buoyancy. Droplets can also roll along the longitudinal direction of the same capillary with curvature comparable to that of the droplet. We have also tested droplet rolling on textured surfaces using PDMS replicas of diffraction gratings (Fig. S7 and Movie S9). Tractions as high as 0.85, approaching the limit of dry friction with no slip, were measured here due to droplet compliance and Hertzian contact with the substrate leading to minimal liquid flux within the gap. These results demonstrate both the significant potential of soft μ bots and how μ bot and substrate properties can profoundly impact μ bot rolling."

We note the Young's moduli of soft droplets are comparable to those of biological cells/tissues and orders of magnitude smaller than other types of soft µbots based on elastomeric composites (Table S1); therefore, we expect no damage to tissues or

blood vessels. These µbots are stable in standard phosphate-buffered saline solutions (pH 7.4 and high salt concentrations) but can also be destabilized when the pH changes to 12 (Movie S10). We also note that the translation speed of soft droplet-based rollers is lower than the rigid µbots we have previously studied (20). This is due to the availability of magnetic particle loading only at the droplet interface, resulting in an overall smaller magnetic torque and leading to a tradeoff between droplet size, which dictates drugloading capacity, and µbot velocity. In addition, and though we have used pH change to trigger emulsion destabilization, alternative methods to destabilize surface particles, such as light or magnetic field-induced hyperthermia (44), are also possible.

Conclusions

We demonstrate the rolling of liquid Pickering emulsion droplets as soft µbots. Compared with their rigid counterparts, soft droplets have higher traction due to the greater friction force associated with their surface deformation and the larger Hertzian-like contact areas with adjacent wall surfaces. Moreover, we can use magnetic fields to reconfigure the particle distribution over the droplet surface when the droplets are partially covered. Under an AC field, particles accumulate at the poles while they redistribute toward the equator when a DC field is added orthogonally. As a result, the translation speed and traction can be tuned over a wide range depending on surface particle configurations. Finally, we have shown that soft µbots can be triggered by pH change to destabilize and release cargo due to the departure of particles from the interface into the aqueous phase. Our work reveals the difference between deformable and rigid

μbots in rolling, demonstrating the potential advantages of using soft μbots for cargo encapsulation, transport, and delivery.

Materials and methods

Materials. Superparamagnetic Dynabeads Myone® carboxylic acid (ThermoFisher Scientific, $2a = 1 \mu m$, carboxylic acid functionalized, particle concentration = 10 mg/ml, zeta potential = -60 mV), 1-ethyl-3-(3-dimethyl aminopropyl) carbodiimide hydrochloride (EDC), n-hydroxysuccinimide (NHS), decane, Pluronic® F-127, and decylamine were purchased from Sigma Aldrich and used as received. Dimethyl sulfoxide (DMSO, $\geq 99.7\%$) and ethanol (200 proof) were purchased from Fisher Scientific and used as received. 184 Silicon Elastomer Kit was purchased from Dow Inc., SYLGARDTM, and used as received. Oil-based ferrofluids EMG 900 was purchased from FerroTec.

Synthesis of amphiphilic particles and fabrication of Pickering emulsions. Before surface modification, 400 μl Dynabead solution from the stock solution was washed with DMSO to remove residual water and surfactants. To activate the carboxyl functional groups, we mixed this solution with 50 ml DMSO and reacted with EDC/NHS (3.8 mg/ml / 2.3 mg/ml) reagents for 4 hr. We then added 0.24 μl decylamine to modify the Dynabead surfaces with alkyl chains for 24 hr. After surface modification, the Dynabeads were washed with DMSO 3×, ethanol 2×, and water 2×, after which the modified Dynabeads were dispersed in DI water at a concentration of 1 mg/ml. Finally, to make stable Pickering emulsions, we added 400 – 800 μl decane to the 5 ml aqueous Dynabead (particle concentration 1 wt%) solution and agitated the mixture for 2 min.

Fabrication of rigid Pickering spheres and soft ferrofluid droplets. We first mixed 1 ml PDMS precursor and curing agent (4:1 by weight) with 1 ml hexane. The mixture was then added to a 5 ml modified Dynabead aqueous solution (1 wt%). After vortex mixing for 2 min, stable Pickering emulsions with a PDMS liquid core and hexane were fabricated. After evaporating hexane in the resulting emulsions, we subsequently heated the emulsions at 70 °C for 1 hr to cure the PDMS. This process yielded Dynabead-coated and rigid PDMS spheres of approximately the same size as the Pickering droplets with a decane liquid core. Sucrose solutions with different concentrations were used to separate the rigid Dynabead-coated Pickering spheres of different densities. The soft ferrofluid droplets were made by emulsifying 400 μl ferrofluids with 10 ml 1 wt% F-127 aqueous solution.

Characterization. The bead zeta potential before and after surface modification was measured with a zeta sizer (Zeta PALS). The morphologies of rigid Pickering spheres with solid PDMS cores were characterized by scanning electron microscopy (JOEL 700FESEM). On an Olympus IX 70 optical microscope, the translational and rotational speeds of soft droplets and rigid spheres were measured based on images captured by a black and white camera (EPIX Inc., SV643M) at 50 frames/s. The rotation of spheres was measured by tracking surface defects.

Magnetic field setup. The magnetic field was generated by four orthogonal copper solenoid coils (Fig. S3) with 51 mm length, 50 mm inner diameter, and 200 or 400 turns. All coils were installed on an aluminum crossing frame (38). One coil with 100 turns, 25 mm length, and 50 mm inner diameter was inserted between four orthogonal coils to apply a field along the *z*-direction. Each coil was connected to an AC or DC power

source, controlled by in-house software (MuControl 1.0.4 version) (45) and an output card (National Instruments, NI-92630). Current detection for each coil was performed through a data acquisition card (NI USB-6009) by measuring the voltage across a 1 Ω resistor (ARCOL, HS150 1 RF) connected in series. The magnetic field strength was measured by an AC/DC Gauss Meter (MF-30K). To generate the 2D rotating magnetic field, we passed a 20 Hz alternating current through each coil oriented along the x and z-directions.

Numerical simulation. The droplets we consider in the numerical simulations are densely coated by particles. Therefore, we treat the droplet surface implicitly and only track the positions of the particles. It is important to note that we do not consider any detailed interfacial hydrodynamics, such as contact line dynamics and meniscus dragging, in our simulations, nor do we account for multiple fluid phases. We simply treat the medium fluid as a bulk with constant viscosity η and use the fast Stokesian dynamics method described in (46) to account for hydrodynamic interactions between particles. This approximation is reasonable because the particles we consider are jammed on the droplet interface and do not move much relative to each other, rendering interfacial corrections to the hydrodynamic mobility higher-order (47,48). Further, the literature has shown that even with the full resolution of a two-phase Stokesian fluid, corrections to the bulk hydrodynamic mobility are typically less than 10% (49).

We express the force balance on the group of particles straddling the surface of the Pickering droplet of radius R as

$$\mathbf{F}^{hydro} + \mathbf{F}^{bend} + \mathbf{F}^{tension} + \mathbf{F}^{mag} + \mathbf{F}^{grav} = 0. \tag{9}$$

The magnetic forces \mathbf{F}^{mag} are used to drive the droplets. The interfacial forces \mathbf{F}^{hydro} , \mathbf{F}^{bend} , and $\mathbf{F}^{tension}$ constrain the particles and capture the droplet softness. The buoyant force \mathbf{F}^{grav} balances \mathbf{F}^{bend} to control deformation against the bottom wall where, for convenience, the droplet is assumed to be heavier than the medium. The hydrodynamic force $\mathbf{F}^{hydro} = \mathbf{M}^{-1}\mathbf{U}$ gives the particle velocities in the suspension through the mobility matrix \mathbf{M} . In our simulations, \mathbf{M} is calculated using lubrication corrections to accurately resolve both near and far-field interactions between particle pairs and a bottom wall (46).

To calculate the interfacial forces F^{hydro} and F^{bend} on the particles, we use their positions in space as the vertices of a triangulated surface mesh representing the droplet. This surface mesh is recalculated at every timestep using the 'ball pivoting' algorithm (50) to avoid significant mesh distortion as the colloids are displaced. Ball pivoting requires an estimation of the normal vector at each vertex or colloid position in our case, so at time t, we use the mesh from time $t - \Delta t$ to estimate the vertex normals as an area-weighted average of the nearest one-ring face-valued normals with the mesh given explicitly for the first step.

The surface mesh allows us to calculate bending/tension forces which mimic the interfacial forces given the particle positions X_i , $i = 1, ..., N_p$. Specifically, we use the discrete bending force described by (51)

$$\boldsymbol{F}_{i}^{bend}(t) = \frac{-\partial}{\partial \boldsymbol{X}_{i}} \sum_{i}^{N_{p}} \frac{\kappa_{bend}}{2} \left(\frac{\|\boldsymbol{C}_{i}\|}{A_{i}(t)} \right)^{2} A_{i}(t)$$
 (10)

and a slightly modified version of the surface tension force

$$\mathbf{F}_{i}^{tension}(t) = \sigma(1.0 - A_{i}(t)/A_{i}^{0})\mathbf{C}_{i} \tag{11}$$

$$\boldsymbol{F}_{i}^{tension}[\boldsymbol{X}_{i}](t) = \frac{-\partial}{\partial \boldsymbol{X}_{i}} \sum_{i}^{N_{p}} \frac{\sigma}{2} \left(\frac{A_{i}(t) - A_{i}^{0}}{A_{i}^{0}} \right)^{2} A_{i}^{0}. \tag{12}$$

In the above equations, $A_i(t)$ is the vertex area at node i and time t; A_i^0 is vertex area at node i and time t = 0; C_i is the mean curvature normal at node i and time t; κ_{bend} is the bending modulus of the droplet, which is treated as a control parameter; $\sigma \propto k_B T \, N_p / 8 \, \pi R^2$ is a penalty parameter used to enforce a constant surface area on the droplets as an effective surface tension and $k_B T$ is the thermal energy at 25°C. σ is chosen to be large enough that the surface area changes by less than 1% over the length of a simulation and small enough that a reasonable time step size can be used.

Particles on the surface of the droplets are packed densely enough to be nearly jammed. To capture this effect, we include spring forces between neighboring particles with rest lengths determined by the particle spacing at t = 0 and stiffness $\kappa_s = 2k_BT$. These spring forces also act to regularize the droplet mesh in time and prevent unphysical shearing or large local area deformations. It has been shown that particles on a fluid interface tend not to rotate from an applied torque (52). We capture this effect by imposing a strong penalty torque on each particle of the form

$$\boldsymbol{\tau}_i^{align} = C\sigma r_p(\boldsymbol{\hat{n}}_i \times \boldsymbol{D}_i^3) \tag{13}$$

where D_i^3 is one component of the orthonormal triad representing the i^{th} particle's orientation (here, the third component is used for consistency with our past work on filaments (53)), \mathbf{n}_i is the i^{th} vertex normal of the mesh, $r_p = 0.5 \, \mu \text{m}$ is the radius of a colloid, and C = 8 is the strength of the penalty.

as

Following prior work(53), we model the magnetic forces between particle i and j

$$\boldsymbol{F}_{ij}^{mag} = \frac{F_0}{r_{ij}^4} \left[2(\overline{\boldsymbol{m}} \cdot \boldsymbol{r}_{ij}) \overline{\boldsymbol{m}} - \left(5(\overline{\boldsymbol{m}} \cdot \boldsymbol{r}_{ij})^2 - 1 \right) \boldsymbol{r}_{ij} \right]$$
(14)

where $F_0 = 3\mu_s m_0^2/4 \pi r_p^4$, $\hat{r}_{ij} = r_{ij}/r_p$, $m_0 = V_0 \chi' H_0$, $V_0 = 4\pi r_p^3 f/3$, f is the fraction of the particle that is paramagnetic, and $\overline{m} = m/m_0$ is the dimensionless magnetic moment of the particle. For the simulations presented in this work we take $F_0 = 1.75 \times 10^{-12} N$, based on our actual experimental conditions. The complex part of the magnetic susceptibility χ'' generates a magnetic torque on particle i(54)

$$\boldsymbol{\tau}_{i}^{mag} = \tau_{0} \hat{\boldsymbol{y}} = \frac{4\pi r_{p}^{3}}{3\mu_{s}} B_{0}^{2} \chi^{"} \hat{\boldsymbol{y}}. \tag{15}$$

Given that the particles on the surface of the droplets are constrained to effectively not rotate, the torque applied to them through the magnetic field gets translated into an effective tangential force of the form

$$\boldsymbol{F}_{i}^{\tau,mag} = \frac{r_{0}}{r_{p}} \boldsymbol{h}_{i} \times \boldsymbol{\hat{y}}. \tag{16}$$

All parameters used in the numerical simulations are listed in Table 1.

Table 1: Parameters and values used in the simulations.

| Parameter | Value | Unit |
|---|--------------|--------------|
| Viscosity, η | 10-3 | Pa·s |
| Particle radius, r_p | 0.5 | μm |
| Drop radius, R | 4.6-19.8 | μm |
| Buoyant force, $N_{\rm p}m_{\rm e}g$ | 83.5 - 331.5 | pN |
| Magnetic force, F_0 | 1.75 | pN |
| Magnetic torque, τ_0 | 0.435 | аJ |
| Effective Surface tension, σ | 17.6 | $aJ/\mu m^2$ |
| Bending modulus, κ_{bend} | 41.7 - 228.3 | aJ |

The error bars for markers along the solid black curve shown in Fig. 3B are calculated using traction values from droplets with the same \bar{a} but different values of κ_{bend} and $m_{\text{e}}g$. Specifically, the lower bound of the error bar corresponds to droplets with a

25% reduction in buoyant force and 25% increase in bending force, while the upper

bound of the error bar corresponds to droplets with a 25% increase in buoyant force and

25% decrease in bending force. The low variance in the error bars demonstrates that

droplet traction is primarily controlled by the dimensionless softness \overline{a} . Due to

computational constraints, error bars for markers along the dashed line (those measuring

the effect of increased drop radius on traction) are calculated conservatively by

measuring the relative percentage difference between two droplets with \bar{a} =2.60, R=11.66

 μm , $\kappa_{\text{bend}} = 59.73$, 238.91 aJ, and $m_{\text{e}g} = 119.46$, 477.82 pN, and then using this percentage

difference as the error for all markers along the dashed line. A 4x disparity in

bending/buoyant forces was used here to ensure conservative error bars with a resulting

relative traction difference = $2|\gamma_1 - \gamma_2|/|\gamma_1 + \gamma_2| = 3.7\%$.

Acknowledgments

We thank Prof. John Brady for insightful discussions on the lubrication of soft

microrobots, Mr. Yuanxing Zhang for helping calculate the magnetic energies of

different surface configurations and Mr. Coy J. Zimmermann for magnetic field setup

building.

Funding: National Science Foundation grant CBET-1762616.

Author contributions:

Conceptualization: DWMM, WN

Methodology: YG, ES, DWMM, WN

Investigation: YG, ES

Simulation: BS

Funding acquisition: DWMM, WN

Writing – original draft: YG, BS, DWMM, WN

Writing – review & editing: BS, DWMM, WN

Competing interests: Authors declare that they have no competing interests.

28

Data and materials availability: All data are available in the main text or the supplementary materials.

Supplementary Materials

Materials and Methods

Figs. S1 to S7 for multiple supplementary figures

Movies S1 to S10 for multiple supplementary movies

References

- 1. P. Erkoc, I. C. Yasa, H. Ceylan, O. Yasa, Y. Alapan and M. Sitti, Mobile microrobots for active therapeutic delivery. *Advanced Therapeutics* **2**, 1800064 (2019).
- 2. J. Wang, W. Gao, Nano/microscale motors: biomedical opportunities and challenges. *ACS Nano* **6**, 5745-5751 (2012).
- 3. D. Li, Y. Liu, Y. Yang, Y. Shen, A fast and powerful swimming microrobot with a serrated tail enhanced propulsion interface. *Nanoscale* **10**, 19673-19677 (2018).
- 4. H. Ceylan, J. Giltinan, K. Kozielski, M. Sitti, Mobile microrobots for bioengineering applications. *Lab on a Chip* **17**, 1705-1724 (2017).
- 5. X. Yang, N. Wu, Change the collective behaviors of colloidal motors by tuning electrohydrodynamic flow at the subparticle level. *Langmuir* **34**, 952-960 (2018).
- 6. F. Ma, S. Wang, D. T. Wu, N. Wu, Electric-field—induced assembly and propulsion of chiral colloidal clusters. *Proceedings of the National Academy of Sciences* **112**, 6307-6312 (2015).
- 7. H. Zeng, P. Wasylczyk, D. S. Wiersma, A. Priimagi, Light robots: bridging the gap between microrobotics and photomechanics in soft materials. *Advanced Materials* **30**, 1703554 (2018).
- 8. F. Cheng, R. Yin, Y. Zhang, C.-C. Yen, Y. Yu, Fully plastic microrobots which manipulate objects using only visible light. *Soft Matter* **6**, 3447-3449 (2010).
- 9. A. Aghakhani, O. Yasa, P. Wrede, M. Sitti, Acoustically powered surface-slipping mobile microrobots. *Proceedings of the National Academy of Sciences* **117**, 3469-3477 (2020).
- 10. X. Lu, K. Zhao, W. Liu, D. Yang, H. Shen, H. Peng, A human microrobot interface based on acoustic manipulation. *Acs Nano* 13, 11443-11452 (2019).
- 11. K. J. Widder, A. E. Senyei, D. F. Ranney, In vitro release of biologically active adriamycin by magnetically responsive albumin microspheres. *Cancer Research* **40**, 3512-3517 (1980).
- 12. K. Leong, J. Kost, E. Mathiowitz, R. Langer, Polyanhydrides for controlled release of bioactive agents. *Biomaterials* 7, 364-371 (1986).

- 13. D. Jin, L. Zhang, Collective Behaviors of Magnetic Active Matter: Recent Progress toward Reconfigurable, Adaptive, and Multifunctional Swarming Micro/Nanorobots. *Accounts of Chemical Research* 55, 98-109 (2021).
- 14. F. Qiu, S. Fujita, R. Mhanna, L. Zhang, B. R. Simona, B. J. Nelson Magnetic helical microswimmers functionalized with lipoplexes for targeted gene delivery. *Advanced Functional Materials* **25**, 1666-1671 (2015).
- 15. C. E. Sing, L. Schmid, M. F. Schneider, T. Franke, A. Alexander-Katz, Controlled surface-induced flows from the motion of self-assembled colloidal walkers. *Proceedings of the National Academy of Sciences* **107**, 535-540 (2010).
- 16. R. Dreyfus, J. Baudry, M. L. Roper, M. Fermigier, H. A. Stone and J. Bibette Microscopic artificial swimmers. *Nature* **437**, 862-865 (2005).
- 17. J. Cui, T.-Y. Huang, Z. Luo, P. Testa, H. Gu, X.-Z. Chen, Nanomagnetic encoding of shape-morphing micromachines. *Nature* **575**, 164-168 (2019).
- 18. H. Xie, M. Sun, X. Fan, Z. Lin, W. Chen, L. Wang, Reconfigurable magnetic microrobot swarm: Multimode transformation, locomotion, and manipulation. *Science Robotics* 4, eaav8006 (2019).
- 19. T. O. Tasci, D. Disharoon, R. M. Schoeman, K. Rana, P. S. Herson, D. W. Marr. Enhanced fibrinolysis with magnetically powered colloidal microwheels. *Small* 13, 1700954 (2017).
- 20. T. Tasci, P. Herson, K. Neeves, D. Marr, Surface-enabled propulsion and control of colloidal microwheels. *Nature Communications* 7, 1-6 (2016).
- 21. A. J. Goldman, R. G. Cox, H. Brenner, Slow viscous motion of a sphere parallel to a plane wall—I Motion through a quiescent fluid. *Chemical Engineering Science* 22, 637-651 (1967).
- 22. D. Ahmed, C. Dillinger, A. Hong, B. J. Nelson, Artificial acousto-magnetic soft microswimmers. *Advanced Materials Technologies* **2**, 1700050 (2017).
- 23. X. Chen, M. Fan, H. Tan, B. Ren, G. Yuan, Y. Jia, Magnetic and self-healing chitosan-alginate hydrogel encapsulated gelatin microspheres via covalent crosslinking for drug delivery. *Materials Science and Engineering: C* **101**, 619-629 (2019).
- 24. Y. Zhao, J. Fang, H. Wang, X. Wang, T. Lin, Magnetic liquid marbles: manipulation of liquid droplets using highly hydrophobic Fe3O4 nanoparticles. *Advanced Materials* 22, 707-710 (2010).
- 25. C. Hu, S. Pané, B. J. Nelson, Soft Micro- and Nanorobotics. *Annual Review of Control, Robotics, and Autonomous Systems* 1, 53-75 (2018).
- 26. X. Fan, M. Sun, L. Sun, H. Xie, Ferrofluid droplets as liquid microrobots with multiple deformabilities. *Advanced Functional Materials* **30**, 2000138 (2020).
- 27. X. Fan, X. Dong, A. C. Karacakol, H. Xie, M. Sitti, Reconfigurable multifunctional ferrofluid droplet robots. *Proceedings of the National Academy of Sciences* **117**, 27916-27926 (2020).
- 28. C. a. Rigoni, J. Fresnais, D. Talbot, R. Massart, R. Perzynski, J.-C. Bacri, Magnetic field-driven deformation, attraction, and coalescence of nonmagnetic aqueous droplets in an oil-based ferrofluid. *Langmuir* **36**, 5048-5057 (2020).

- 29. X. Liu, N. Kent, A. Ceballos, R. Streubel, Y. Jiang, Y. Chai, Reconfigurable ferromagnetic liquid droplets. *Science* **365**, 264-267 (2019).
- 30. C. Tao, T. Chen, H. Liu, S. Su, Design of biocompatible Fe3O4@ MPDA mesoporous core-shell nanospheres for drug delivery. *Microporous and Mesoporous Materials* **293**, 109823 (2020).
- 31. S. Melle, M. Lask, G. G. Fuller, Pickering emulsions with controllable stability. *Langmuir* **21**, 2158-2162 (2005).
- 32. K. Zhang, W. Wu, K. Guo, J.-F. Chen, P.-Y. Zhang, Magnetic polymer enhanced hybrid capsules prepared from a novel Pickering emulsion polymerization and their application in controlled drug release. *Colloids and Surfaces A: Physicochemical and Engineering Aspects* **349**, 110-116 (2009).
- 33. L. E. Low, L. T.-H. Tan, B.-H. Goh, B. T. Tey, B. H. Ong and S. Y. Tang, Magnetic cellulose nanocrystal stabilized Pickering emulsions for enhanced bioactive release and human colon cancer therapy. *International Journal of Biological Macromolecules* **127**, 76-84 (2019).
- **34**. E. Dintwa, E. Tijskens, H. Ramon, On the accuracy of the Hertz model to describe the normal contact of soft elastic spheres. *Granular Matter* **10**, 209-221 (2008).
- 35. T. Supakar, A. Kumar, J. Marston, Impact dynamics of particle-coated droplets. *Physical Review E* **95**, 013106 (2017).
- 36. B. Wu, C. Yang, Q. Xin, L. Kong, M. Eggersdorfer, J. Ruan, Attractive Pickering Emulsion Gels. *Advanced Materials* **33**, 2102362 (2021).
- 37. S. Krijt, C. Dominik, A. G. G. M. Tielens, Rolling friction of adhesive microspheres. *Journal of Physics D: Applied Physics* **47**, 175302 (2014).
- 38. T. Yang, T. O. Tasci, A. Tomaka, N. Wu, D. W. M. Marr, Microwheels on microroads: Enhanced translation on topographic surfaces. *Science Robotics* 4, eaaw9525 (2019).
- 39. Z. Wang (2011) Polydimethylsiloxane Mechanical Properties Measured by Macroscopic Compression and Nanoindentation Techniques. (University of South Florida, Ann Arbor), p 78.
- 40. M. H. Essink, A. Pandey, S. Karpitschka, C. H. Venner, J. H. Snoeijer, Regimes of soft lubrication. *Journal of Fluid Mechanics* **915**, A49 (2021).
- 41. V. A. Dahl, A. B. Dahl, R. Larsen, in 2014 2nd International Conference on 3D Vision. (IEEE, 2014), vol. 2, pp. 82-89.
- 42. M. t. Hart, The projection point geodesic grid algorithm for meshing the sphere. *J. Comput. Phys.* **454**, 33 (2022).
- 43. N. Deirram, C. Zhang, S. S. Kermaniyan, A. P. Johnston, G. K. Such, pH-responsive polymer nanoparticles for drug delivery. *Macromolecular Rapid Communications* **40**, 1800917 (2019).
- 44. S. Sharma, N. Shrivastava, F. Rossi, N. T. K. Thanh, Nanoparticles-based magnetic and photo induced hyperthermia for cancer treatment. *Nano Today* **29**, 100795 (2019).

- 45. E. Roth, C. Zimmermann, D. Disharoon, T. Tasci, D. Marr, K. Neeves, An experimental design for the control and assembly of magnetic microwheels. *Review of Scientific Instruments* **91**, 093701 (2020).
- 46. B. Sprinkle, E. B. Van Der Wee, Y. Luo, M. M. Driscoll, A. Donev, Driven dynamics in dense suspensions of microrollers. *Soft Matter* **16**, 7982-8001 (2020).
- 47. A. Dani, G. Keiser, M. Yeganeh, C. Maldarelli, Hydrodynamics of particles at an oil—water interface. *Langmuir* **31**, 13290-13302 (2015).
- 48. A. Dani, M. Yeganeh, C. Maldarelli, Hydrodynamic Interactions Between Charged and Uncharged Brownian Colloids at a Fluid-Fluid Interface. *arXiv* preprint *arXiv*:2203.13925, (2022).
- 49. J.-C. Loudet, M. Qiu, J. Hemauer, J. Feng, Drag force on a particle straddling a fluid interface: Influence of interfacial deformations. *The European Physical Journal E* **43**, 1-13 (2020).
- 50. F. Bernardini, J. Mittleman, H. Rushmeier, C. Silva, G. Taubin, The ball-pivoting algorithm for surface reconstruction. *IEEE transactions on visualization and computer graphics* **5**, 349-359 (1999).
- 51. C.-H. Wu, T. G. Fai, P. J. Atzberger, C. S. Peskin, Simulation of osmotic swelling by the stochastic immersed boundary method. *SIAM Journal on Scientific Computing* **37**, B660-B688 (2015).
- 52. W. Fei, P. M. Tzelios, K. J. Bishop, Magneto-capillary particle dynamics at curved interfaces: time-varying fields and drop mixing. *Langmuir*, (2020).
- 53. T. Yang, B. Sprinkle, Y. Guo, J. Qian, D. Hua, A. Donev, D.WM.Marr, N. Wu, Reconfigurable microbots folded from simple colloidal chains. *Proceedings of the National Academy of Sciences* **117**, 18186-18193 (2020).
- 54. X. Zhu, Y. Gao, R. Mhana, T. Yang, B. L. Hanson, X. Yang, N. Wu, Synthesis and Propulsion of Magnetic Dimers under Orthogonally Applied Electric and Magnetic Fields. *Langmuir* 37, 9151-9161 (2021).